Ice Templated Free-Standing Hierarchically WS_2/CNT-rGO Aerogel for High-Performance Rechargeable Lithium and Sodium Ion Batteries

*Ye Wang, Dezhi Kong, Wenhui Shi, Bo Liu, Glenn Joey Sim, Qi Ge, and Hui Ying Yang**

A hybrid nanoarchitecture aerogel composed of WS_2 nanosheets and carbon nanotube-reduced graphene oxide (CNT-rGO) with ordered microchannel three-dimensional (3D) scaffold structure was synthesized by a simple solvothermal method followed by freeze-drying and post annealing process. The 3D ordered microchannel structures not only provide good electronic transportation routes, but also provide excellent ionic conductive channels, leading to an enhanced electrochemical performance as anode materials both for lithium-ion batteries (LIBs) and sodium-ion batteries (SIBs). Significantly, WS_2/CNT-rGO aerogel nanostructure can deliver a specific capacity of 749 mA h g^{-1} at 100 mA g^{-1} and a high first-cycle coulombic efficiency of 53.4% as the anode material of LIBs. In addition, it also can deliver a capacity of 311.4 mA h g^{-1} at 100 mA g^{-1}, and retain a capacity of 252.9 mA h g^{-1} at 200 mA g^{-1} after 100 cycles as the anode electrode of SIBs. The excellent electrochemical performance is attributed to the synergistic effect between the WS_2 nanosheets and CNT-rGO scaffold network and rational design of 3D ordered structure. These results demonstrate the potential applications of ordered CNT-rGO aerogel platform to support transition-metal-dichalcogenides (i.e., WS_2) for energy storage devices and open up a route for material design for future generation energy storage devices.

1. Introduction

Recently, high performance energy storage devices have gained attention in industrial and research communities as a result of the exponentially increasing market demand of the portable electronic devices and electric vehicles.[1–4] Among numerous energy storage devices, rechargeable lithium ion batteries (LIBs) and sodium ion batteries (SIBs) are two major groups due to their high energy densities, nonmemory effect, environmental friendly technology, and long cycle life.[5–7] In addition, SIBs own a high potential in smart-grid applications due to the high abundance nature resources and low cost of sodium.[8,9] However, the further development of both LIBs and SIBs is impeded by the facts of the relatively low specific capacity and large volume change during the charging/discharging process. The relative high inner resistivity could lead to inferior electrochemical performance, including low rate capability and cycle stability.[10,11] As the radius of sodium ions is larger than that of lithium ions (≈0.106 nm for sodium ions vs ≈0.076 nm for lithium ions), these challenges are even greater for SIBs.[12,13] Therefore, high performance materials and effective structure design are obviously critical to solve the bottleneck faced by LIBs and SIBs.[14–19]

2D transition metal dichalcogenides (TMDs) have been recognized as promising active materials for LIBs and SIBs owing to their unique physical and electrochemical properties.[20,21] Compared with conventional metal oxides for LIBs or SIBs, metal sulfides have better ion transportation through their larger interlayer spacing and higher conductivity.[22] WS_2, one of 2D TMDs, shows its great advantageous features used as the anode of LIBs. On the one hand, WS_2 has a relatively higher theoretical specific capacity of 432 mA h g^{-1} than that of graphite which is used as the commercial anode of LIBs.[23] On the other hand, WS_2 has a large interlayer spacing of (002) facial (d = 0.62 nm) and weak van der Waals interaction, which allows the Li^+/Na^+ ions to diffuse without a significant volume change to keep the structure stable during the lithium or sodium ions insertion/desertion.[24] Although MoS_2 has been extensively studied as the anode for both LIBs and SIBs, WS_2, which has a higher intrinsic electronic conductivity than that of MoS_2, has not been studied in the applications of both LIBs and SIBs.[25,26]

General strategies to improve the kinetic performance of lithium or sodium ions with WS_2 electrodes include: (a) synthesis nanosize structure to reduce the diffusion length of lithium or sodium ions,[15,27] and (b) incorporation with carbonaceous materials as the supporting matrix to increase the conductivity and reduce the volume change during the lithiation/delithiation or sodiation/desodiation process.[11,17,28] In addition, plenty of investigations found that electrode architecture has great impact on the device performance. For example, 3D bicontinuous carbon based network is of great interests due to the excellent electronic conductivity (electronic conductor)

Dr. Y. Wang, Dr. D. Kong, Dr. W. Shi, B. Liu, G. J. Sim, Prof. Q. Ge, Prof. H. Y. Yang
Pillar of Engineering Product Development
Singapore University of Technology and Design
8 Somapah Road, 487372, Singapore
E-mail: yanghuiying@sutd.edu.sg

DOI: 10.1002/aenm.201601057

and ionic conductivity (pore structure).[29,30] Highly ordered 3D electrodes have been fabricated by a template assisted approach with additional chemicals involved (PS spheres, for instance), leading to process complexity and high cost.[31] Importantly, the template free method would introduce random pores which degrade the interpenetration of electrolyte into the network. Therefore, as a very unique template, ice-templating method (also called ice segregation induced self-assembly) without additional chemical involved is highly desired to form the ordered carbon based microstructure by simple fast unidirectional freezing and freeze-drying process.[32,33]

In this work, WS_2/carbon nanotube-reduced graphene oxide (WS_2/CNT-rGO) aerogels with ordered microchannel 3D structure were synthesized through a simple solvothermal method and ice-template assisted post freeze drying process. WS_2/CNT-rGO aerogel nanostructure was further used as the anode electrode directly for both LIBs and SIBs without additional binder and conductive agent. Such unique 2D/3D (2D: WS_2 nanosheets, 3D: CNT-rGO scaffold aerogel) hybrid hierarchical nanoarchitecture design offers several merits for energy storage. First, ultrathin WS_2 nanosheets provide a large surface area and defect sites, which can effectively reduce the lithium/sodium ion diffusion length and increase electrolyte ion accessibility. Second, WS_2 nanosheets grown in the network of CNT and supported by rGO network architecture, CNT-rGO aerogel not only acts as the matrix to support WS_2 nanosheets to prevent mechanical peeling off from the electrode and the restacking issue during the cycling, but also provides better electronic conductivity to improve the electron transportation. Third, the ordered microchannel 3D network structures created by the CNT-rGO aerogel may enhance the wetability of the electrolyte and increase the contact sites between electrolyte and WS_2 active materials. Fourth, free-standing and binder free electrode design further reduce the weight of electrode for full battery, and prevent the additional capacity originated from the conductive agents, as well as the electrode deterioration during the lithiation/sodiation process.[12] Owing to these advantages, the synthesized binder free WS_2/CNT-rGO aerogel hybrid nanoarchitecture electrodes show outstanding performance not only for LIBs, but also for SIBs.

2. Results and Discussion

2.1. Morphology and Structure of WS_2/CNT-rGO Aerogel Nanostructures

The synthesis procedure of WS_2/CNT-rGO aerogel nanoarchitecture is schematically shown in **Figure 1**. First, GO, CNT, and $(NH_4)_2WS_4$ powder were mixed and dissolved in 20 mL N,N-dimethyformamide (DMF) by probe sonication and stirred homogeneously. WS_4^{2-} ions started to form nanosheets sandwiched with CNT at the beginning of the solvothermal process.[34] During the high temperature and high pressure solvothermal reaction, due to the π–π stacking between graphene oxide sheets, GO and CNT/WS_2 formed 3D network, as shown in step 2.[35] During this process, GO was reduced into rGO by the thermal reduction.[36] After the hydrogel collected from the autoclave, the hydrogel sample was washed by DMF and deionized (DI) water to remove the unreacted chemicals and solvent. Then the sample was put into the liquid nitrogen for several minutes for fast unidirectional freezing, followed by transferring into the freeze dryer and treated for 48 h, as shown in step 3. During the freezing stage (in liquid nitrogen),

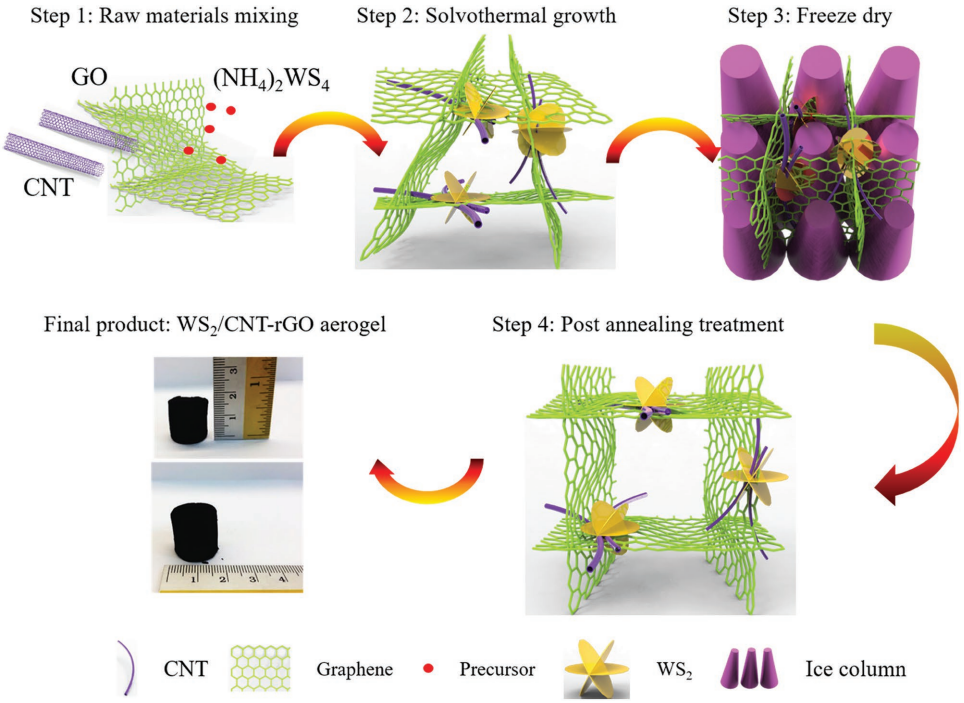

Figure 1. Schematic diagram of WS_2/CNT-rGO aerogel 3D ordered microchannel nanoarchitecture synthesis process.

ice columns grew starting from the bottom with a diameter of 5–15 μm. With the assistance of ice columns, WS_2/CNT-rGO nanocomposites would reform with new structures follow the surface of ice columns and fixed the shape during the freeze drying process.[32,33] After 48 h of the freeze drying process (high vacuum sublimation of ice columns), the final product was collected after thermal annealing at 500 °C under N_2/H_2 (95%/5%) atmosphere, as indicated in step 4. The aerogel with 200 mg $(NH_4)_2WS_4$ precursor is named as WS_2/CNT-rGO-200. Typical diameter and height of final WS_2/CNT-rGO aerogel are 20 and 18 mm, respectively, as shown in the last image of Figure 1. It is worth mentioning that WS_2 nanosheets can grow on the surface of CNT instead of GO by $(NH_4)_2WS_4$ precursor, as both WS_4^{2-} and GO are negatively charged. As GO is easy to form 3D scaffold aerogel structure during the hydrothermal/solvothermal process, CNT and GO were selected to form the 3D aerogel structure for WS_2.[37] Moreover, CNT also can effectively prevent the restacking of GO during the aerogel formation process.[38] It is also reported that the positively charged cetyltrimethylammonium (CTA) was employed to synthesize WS_2/rGO nanostructure through connecting the negatively charged GO and WS_4^{2-} ions to form WS_4^{2-}-CTA^+-GO complex.[34] However, the involvement of cetyltrimethylammonium bromide (CTAB) surfactant chemicals in the chemical reaction results in additional chemicals usage and process complexity.

Figure 2 presents the morphology of pure CNT-rGO aerogel and WS_2/CNT-rGO-200 aerogel. Ordered microcavities are clearly observed in the CNT-rGO aerogel with a diameter of 5–15 μm (Figure 2a). CNT-rGO walls connect together to form 3D network scaffold structures (Figure 2b). A closer SEM image in Figure 2c shows that rGO as the supporting materials to form a 3D scaffold and CNTs are integrated onto rGO walls. The ordered microcavities are the vacancies after sublimation of ice columns. The cross section of CNT-rGO aerogel shows (Figure S1, Supporting Information) that microchannels are along the longitudinal direction through the aerogel. Ordered microcavity/microchannel structures are also clearly observed in WS_2/CNT-rGO aerogel in Figure 2d. White dots in Figure 2e are WS_2 nanoflowers composed of thin nanosheets embedded inside CNT networks as shown in Figure 2f.

The microstructure of the synthesized nanocomposites was characterized by transmission electron microscopy (TEM) as indicated in **Figure 3**. Figure 3a,b present the typical TEM images of pure CNT-rGO aerogel. CNTs are clearly observed on rGO sheets, which can be distinguished by their wrinkle shapes and edges as indicated by red arrows shown in Figure 3a. A closer observation of the high-resolution TEM (HRTEM) image (Figure 3b) shows that multiwall CNTs (with 10–20 layers) are on the surface of rGO nanosheets. WS_2 nanosheets with a diameter of approximately 200 nm are grown embedded in CNTs on the surface of rGO sheets (Figure 3c). Some nanosheets are grown together to form nanoflower like shape. HRTEM image (Figure 3d) also indicates that WS_2 nanosheets are composed of approximately 20 layers with an inter-planar spacing of 0.63 nm, corresponding to the (002) crystal plane of WS_2.[26]

The material composition and crystal structure of WS_2 powder and WS_2/CNT-rGO aerogels were performed by X-ray diffraction (XRD) patterns, as shown in **Figure 4**a. For the WS_2/CNT-rGO aerogels, strong peaks located at 13.9°, 33.5°, 39.5°, and 59.1° can be indexed as the (002), (100/101), (103), and (110) planes of hexagonal structure of WS_2 (JCPDS card No. 84–1398), respectively, which is consistent with the commercial WS_2 powder and previous reports.[26,39] The peak located at 26° and a tiny peak located at 30.2° are originated from the CNT-rGO (Figure S2, Supporting Information).[40] Raman spectra of commercial WS_2 powder, CNT-rGO aerogel, WS_2/CNT-rGO aerogels are shown in Figure 4b. Two strong Raman peaks located at 351 and 420 cm^{-1} can be attributed to the typical Raman active E_{2g} and A_{1g} vibration modes of WS_2, respectively.[41,42] The peaks at 1351 and 1589 cm^{-1} are corresponding to the D and G bands of CNT-rGO, corresponding to the disorder carbon atoms in the hexagonal graphite network and the in-plane vibrational mode of sp^2-bonded carbon atoms, respectively.[43–45] The peak located at 2722 cm^{-1} should be attributed to 2D band of CNT-rGO carbon.[46] It is also found that the peaks belong to WS_2 become stronger with the

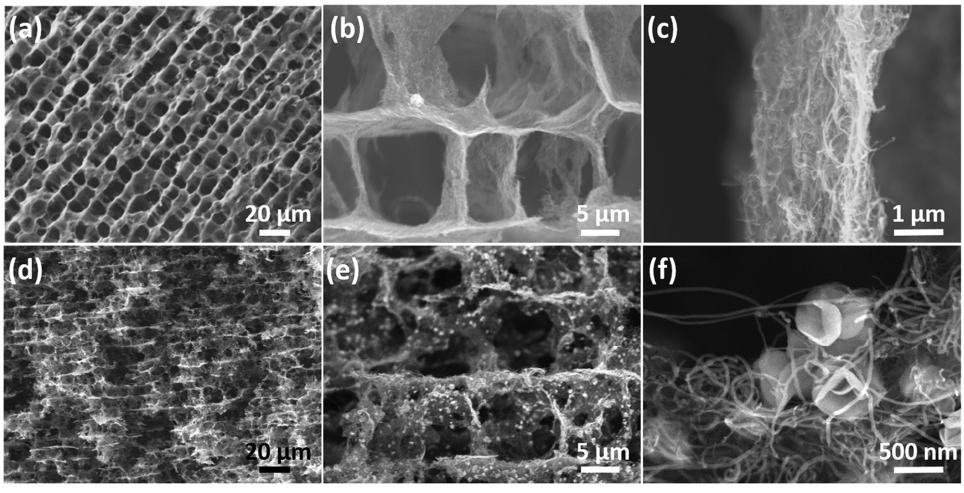

Figure 2. a–c) Various magnifications SEM images of CNT-rGO aerogel with 3D ordered structure. d–f) Various magnifications SEM images of WS_2/CNT-rGO-200 aerogel.

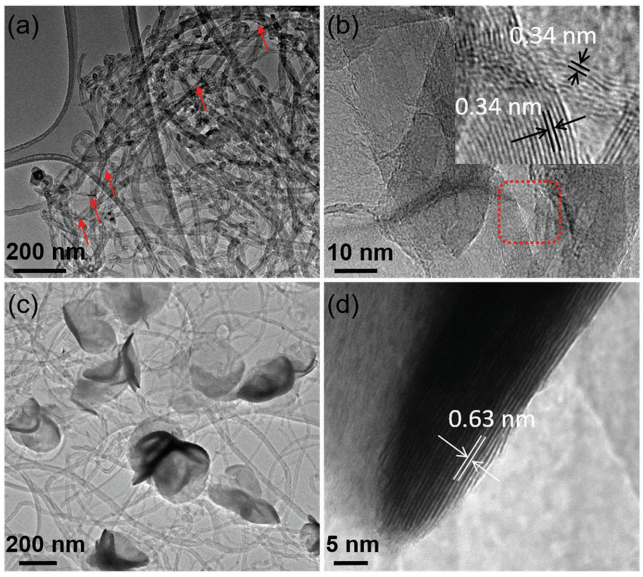

Figure 3. a) TEM and b) HRTEM images of pristine CNT-rGO aerogel. Red arrows indicate the wrinkles and edges of the rGO sheets. Inset in (b) is an enlarged view of the squared area in (b) to show the lattice of CNT and rGO. c) TEM and d) HRTEM images of WS_2 /CNT-rGO-200 aerogel.

increase of WS_2 precursor mass, indicating the loading of WS_2 in WS_2/CNT-rGO aerogel is increased.

The content of WS_2 in hybrid WS_2/CNT-rGO aerogel was measured by thermogravimetric analysis (TGA) in a compressed air atmosphere in the temperature range of room temperature to 1000 °C (Figure S3, Supporting Information). Take WS_2/CNT-rGO-200 aerogel as an example, approximately 1.5% weight loss below 100 °C is due to the evaporation of moisture adsorbed on the surface of the nanostructures.[47] Approximately 48.2% weight loss between 100 and 700 °C should be attributed to the oxidization of functional groups on the surface of the rGO, oxidization of rGO and CNT in the air, and conversion of WS_2 into WO_3.[48–50] Therefore, approximately 50.3% weight total material left after 700 even 1000 °C should be WO_3.[49] According to the theoretical calculation, the weight loss from WS_2 into WO_3 should be approximately 6.4%. Therefore, the WS_2 content in WS_2/CNT-rGO-200 aerogel is 54.3%, and the CNT-rGO is approximately 45.7%. The contents of WS_2 and CNT-rGO in WS_2/CNT-rGO aerogels with various precursor masses are summarized in Table S1 (Supporting Information).

2.2. Lithium Ion Storage Performance

The lithium ion storage performance of WS_2/CNT-rGO aerogel nanocomposites was evaluated in a half-cell battery configuration with the active material, lithium foil and Celgard 2400 membrane as the working electrode, counter electrode and separator, respectively. **Figure 5**a shows the cyclic voltammetry (CV) curves of WS_2/CNT-rGO-200 aerogel with the first five cycles in the potential range of 0.01–3 V (vs Li/Li^+) at a scan rate of 0.1 mV s^{-1}. In the first cathodic process, the peak located approximately at 0.5 V can be attributed to the reduction reaction of WS_2 to metallic W nanoparticles embedded in Li_2S matrix, insertion of Li ions into CNT-rGO, and accompanying with the irreversible decomposition of the electrolyte and formation of the gel like solid electrolyte interface (SEI) layer at the surface of the electrode.[51] The same peak located at 0.5 V for commercial WS_2 powder is also found in the first lithiation process and became very weak during the following cycles (Figure S4a, Supporting Information). In the first anodic scan, a relatively very small peak located at 1.72 V, and a large peak at 2.5 V associated with the oxidation of W to WS_2.[52] In the subsequent cycles, the peaks located at 2.03 and 1.76 V during the lithiation process are usually corresponding to the formation of Li_xWS_2.[52] It is also worth mentioning that the intensity of CV peaks belong to WS_2 is increased and peaks belong to CNT-rGO is decreased with the increase of WS_2 precursor from 0 mg (CNT-rGO) to 300 mg (Figure S4b–d, Supporting Information).

Figure 5b shows the galvanostatic discharge/charge curves of WS_2/CNT-rGO-200 aerogel nanocomposites for the first 10 cycles in the potential range of 0.01–3 V versus Li/Li^+ at a current density of 200 mA g^{-1}. In the first discharge curve, a long plateau located at approximately 0.72 V is related to the conversion reaction of WS_2 into metallic W nanoparticles and Li_2S, and the SEI layer formation.[51,52] In the first charge process, there is a plateau located at 2.2–2.5 V, corresponding to the oxidation of W into WS_2 during the delithiation process.[53] The lithiation and delithiation behaviors are consistent with the CV curves shown in Figure 5a. Compared with the pristine CNT-rGO aerogel and WS_2 commercial powder, WS_2/CNT-rGO aerogels exhibit longer flat plateaus, which can be attributed to the synergistic effect between WS_2 nanosheets and CNT-rGO networks. The specific capacities of the first discharge and charge cycle are 1043.2 and 557.4 mA h g^{-1}, respectively, leading to an initial coulombic efficiency (CE) of 53.4%. The irreversible capacity may be due to the irreversible reaction of the decomposition of electrolyte and the formation of SEI film, which is generally observed in the anode materials.[47,54–56] In the second cycle, the discharge and charge capacities are decreased into 626.7 and 558.4 mA h g^{-1}, respectively, with an

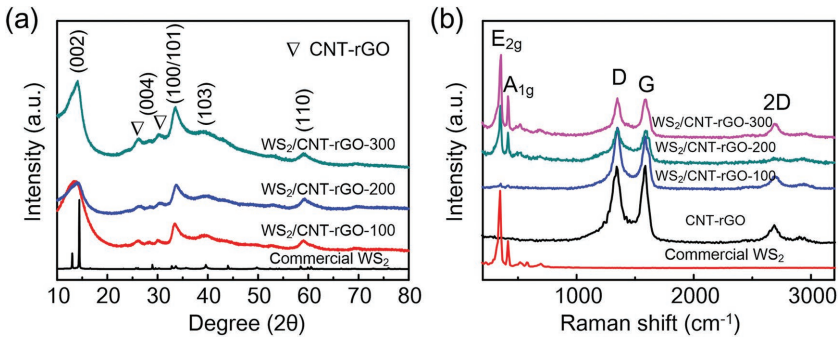

Figure 4. a) XRD patterns of WS_2 commercial powder and WS_2/CNT-rGO aerogels with various precursor masses (100, 200, and 300 mg). b) Raman curves of WS_2 commercial powder, CNT-rGO aerogel, and WS_2/CNT-rGO aerogels with various precursor masses (100, 200, and 300 mg).

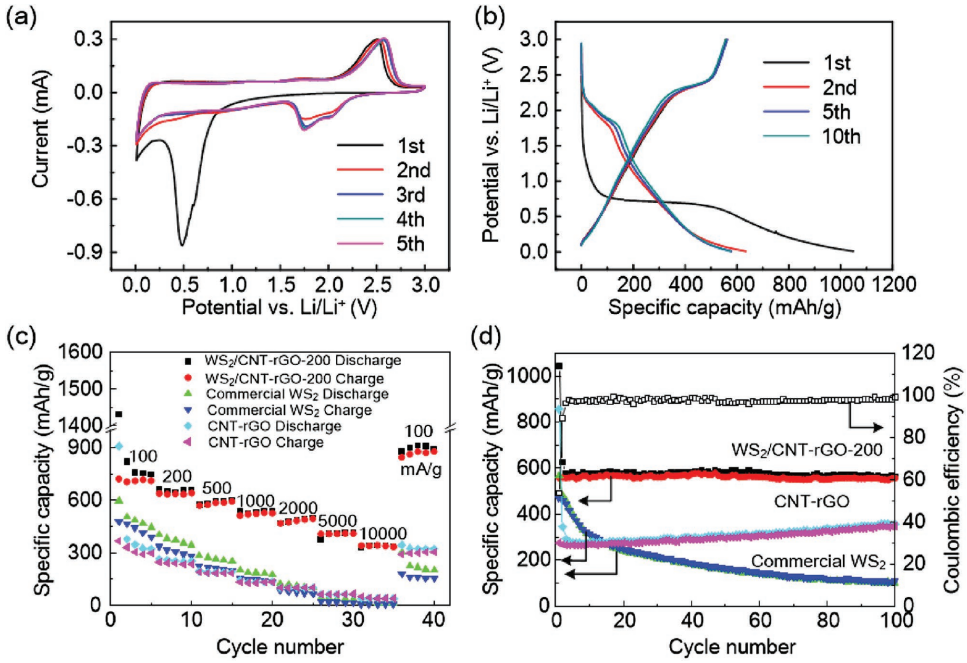

Figure 5. Electrochemical performance of WS_2/CNT-rGO-200 aerogel nanocomposites as the anode materials of LIBs. a) CV curves of the WS_2/CNT-rGO-200 aerogel electrode of the first five cycles at a scan rate of 0.1 mV s^{-1} in a potential range of 0.01–3 V versus Li/Li^+. b) Galvanostatic discharging/charging curves of the WS_2/CNT-rGO-200 aerogel electrode at a current density of 200 mA g^{-1} for the first 10 cycles. c) Rate capability of WS_2/CNT-rGO-200 aerogel, WS_2 commercial powder, and CNT-rGO aerogel electrodes at the current densities ranging from 100 to 10000 mA g^{-1}. d) Cycling performance of WS_2/CNT-rGO-200 aerogel, WS_2 commercial powder, and CNT-rGO aerogel electrodes at a current density of 200 mA g^{-1}, and coulombic efficiency of WS_2/CNT-rGO-200 aerogel electrode.

increased CE of 89.1%. This value is remained higher than 97% in the subsequent cycles. Large CE means high reversible capacities can be delivered during the delithiation process. In addition, a voltage hysteresis of approximately 0.4 V is observed (Figure 5b), which is commonly reported for WS_2 and MoS_2 anode materials of LIBs.[57,58] It can be further reduced by material nanostructure design to change the lithium kinetic behavior at the surface and inside of nanostructures.[59,60]

The rate capacities of WS_2/CNT-rGO-200 aerogel, commercial WS_2 powder and CNT-rGO aerogel electrodes are shown in Figure 5c. Reversible specific capacities of 749, 656, 602, 536, 501, 414, and 337 mA h g^{-1} are achieved for WS_2/CNT-rGO-200 aerogel electrode at the current densities of 100, 200, 500, 1000, 2000, 5000, and 10 000 mA g^{-1}, respectively. It is worth mentioning that the capacity is returned to 878 mA h g^{-1} when the current density is adjusted from 10 000 into 100 mA g^{-1}. By contrast, the specific capacity of commercial WS_2 is only 441 and 11.8 mA h g^{-1} at the current densities of 100 and 10 000 mA g^{-1}, respectively (Figure 5c). It is worth mentioning that the capacity of WS_2 commercial powder is decreased quickly with the increase of current density, leading to an inferior rate capability. With the incorporation of the CNT-rGO, the rate capability of WS_2/CNT-rGO aerogel electrodes is improved as indicated in Figure 5c and Figure S5a,b (Supporting Information). The cycling performance of the WS_2/CNT-rGO-200 aerogel is shown in Figure 5d. It can be seen that WS_2/CNT-rGO-200 aerogel can deliver a discharge (lithiation) capacity of 572 mA h g^{-1} after 100 cycles at a current density of 200 mA g^{-1}, whereas the electrode of commercial WS_2 and pure CNT-rGO aerogel only can deliver capacities of 107 and 355 mA h g^{-1} at the same current density, respectively. On the other hand, WS_2/CNT-rGO electrodes with 100 and 300 mg precursors can deliver capacities of 413 and 469 mA h g^{-1}, respectively (Figure S6a,b, Supporting Information). In addition, the specific capacity of CNT-rGO aerogel is increased with the cycles, this is may be due to the activation process during cycles.[61,62] While WS_2/CNT-rGO-200 aerogel can keep its 99% initial the delithiation (charge) capacity after 100 cycles. In specific, it is increased slightly from 557 mA h g^{-1} (the 1st cycle) to 579 mA h g^{-1} (the 47th cycle), and then decreased very slowly to 556 mA h g^{-1} (the 100th cycle). The increasement for the first 47 cycles is not as prominent as that of the CNT-rGO aerogel, the possible reason is due to the capacity contribution from CNT-rGO (134 mA h $g^{-1}_{WS2/CNT\text{-}rGO\text{-}200}$) is much lower than that of WS_2 (445 mA h $g^{-1}_{WS2/CNT\text{-}rGO\text{-}200}$) (based on the capacity at the 47th cycles, see Supporting Information for the calculation process).

In order to explore the intrinsic electrochemical and kinetic mechanisms of WS_2/CNT-rGO aerogels, the electrochemical impedance spectroscopy (EIS) spectra were measured after the first three cycles, as shown by the Nyquist plots (Figure S7, Supporting Information). The equivalent circuit model shown in the insert in Figure S7 (Supporting Information) is used to simulate the electrical components, where R_s is the current collector and electrolyte resistance; R_f and CPE1 are the SEI layer resistance and the constant phase element, R_{ct} and CPE2 are the charge transfer resistance and constant phase element for double layer capacitor, respectively; and W is the Warburg

impedance related to the lithium diffusion.[63,64] The fitting results are shown in Table S2 (Supporting Information). The charge transfer resistance of the WS_2/CNT-rGO-200 aerogel (286.9 Ω) is much lower than that of commercial WS_2 powder (599.9 Ω), due to the incorporation of conductive agent of CNT-rGO network.

2.3. Sodium Ion Electrochemical Performance

WS_2/CNT-rGO aerogel nanostructures are also used as the anode electrodes of sodium ion batteries (SIBs), and the related electrochemical performance is shown in **Figure 6**. In the first cathodic scan of CV curve of WS_2/CNT-rGO-200 aerogel electrode (Figure 6a), there are two peaks including a weak peak located at 1.2 V and a major peak centered at about 0.57 V in the first sodiation process, they should be attributed to the insertion of sodium ions into WS_2 lattice to form Na_xWS_2, conversion reaction of WS_2 with sodium ions into W metallic nanoparticles embedded into amorphous Na_2S matrix, and the formation of SEI layer at the surface of electrode.[65] In the first anodic scan, there are three peaks located at 1.9, 2.3, and 2.6 V which should be attributed to the oxidation of W to WS_2 during desodiation process.[65–67] The peak positions of WS_2/CNT-rGO-200 aerogel electrode are almost same as that of WS_2 (Figure S8a, Supporting Information) and different from that of the CNT-rGO aerogel (Figure S9a, Supporting Information), indicating that the sodium ion storage ability is mainly contributed from WS_2 nanostructure. Figure 6b shows the galvanostatic discharge/charge curves of WS_2/CNT-rGO-200 aerogel electrode for the first 10 cycles in the potential range of 0.01–3 V versus Na/Na^+ at a current density of 200 mA g^{-1}. In the first discharge curve, the long plateau located at about 1.1–0.6 V is ascribed to sodium ions intercalation into the WS_2 lattice, WS_2 converted into W nanoparticles and the formation of SEI layer.[67] In the first charge process, there are three plateaus including a major plateau located at 1.7–1.9 V and two small plateaus located at 2.3 and 2.6 V, which should be corresponding to the conversion of W into WS_2.[65] These sodiation and desodiation behaviors are consistent with the CV curves shown in Figure 6a. Same as the LIBs performance, WS_2/CNT-rGO aerogel anode electrodes of SIBs also exhibit improved performance than that of pristine CNT-rGO aerogel and WS_2 commercial powder electrode. The specific capacities of the first sodiation and desodiation cycle are 900.8 and 305 mA h g^{-1}, respectively, leading to an initial CE of 33.9%. As mentioned in the LIBs performance part, the irreversible capacity may due to the irreversible reaction of the decomposition of electrolyte and the formation of SEI film.[67] We note that the initial CE of CNT-rGO aerogel electrode is only 25.1% (Figure S9b,d, Supporting Information), this is one of the reasons for the low initial CE of WS_2/CNT-rGO aerogel anode electrode of SIBs. In the second cycle, the discharge and charge capacities are decreased into 328.4 and 294.4 mA h g^{-1}, respectively, with an increased CE of 89.7%. This value is remained higher than 96% in the subsequent cycles.

The rate capability of WS_2/CNT-rGO-200 aerogel nanocomposites is shown in Figure 6c. Reversible specific capacities of 311.4, 302.8, 289, 262.8, 221.1, 129.2, and 47.2 mA h g^{-1} are achieved at current densities of 100, 200, 500, 1000, 2000,

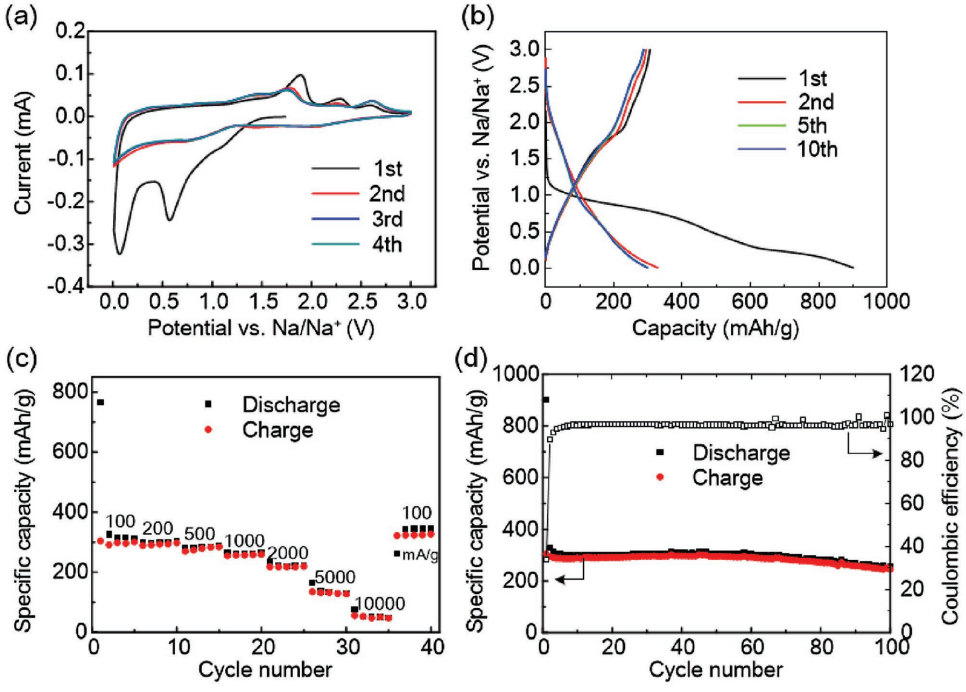

Figure 6. Electrochemical performance of WS_2/CNT-rGO-200 aerogel as the anode electrode of SIBs. a) CV curves of the first four cycles at a scan rate of 0.1 mV s^{-1} in a potential range of 0.01–3 V versus Na/Na^+. b) Galvanostatic discharging/charging curves at a current density of 200 mA g^{-1} for the first 10 cycles. c) Rate capability at the current densities ranging from 100 to 10 000 mA g^{-1}. d) Cycling performance and coulombic efficiency at a current density of 200 mA g^{-1}.

5000, and 10 000 mA g^{-1}, respectively. The capacity is returned to 342.6 mA h g^{-1} when the current density is adjusted from 10 000 into 100 mA g^{-1}. By contrast, the capacities at high current densities of WS_2/CNT-rGO-200 aerogel are much higher than that of both commercial WS_2 powder and pristine CNT-rGO aerogel. For example, commercial WS_2 powder and CNT-rGO aerogel can deliver capacities of 118.1 and 58.5 mA h g^{-1} at a current density of 1000 mA g^{-1}, respectively (Figures S8c and S9c, Supporting Information). The cycling performance of the WS_2/CNT-rGO-200 aerogel electrode is shown in Figure 6d. It can deliver a capacity of 252.9 mA h g^{-1} after 100 cycles at a current density of 200 mA g^{-1}. Whereas commercial WS_2 powder and pure CNT-rGO aerogel deliver capacities of 23.3 and 61.4 mA h g^{-1} after 100 cycles, respectively (Figures S8d and S9d, Supporting Information). WS_2/CNT-rGO-100 and WS_2/CNT-rGO-300 aerogel electrodes deliver discharge capacities of 54.2 and 99.7 mA h g^{-1} after 100 cycles, respectively (Figures S10d and S11d, Supporting Information). It is also noted that the capacity of WS_2 commercial powder is degraded quickly with the cycles. However, the stability of WS_2/CNT-rGO aerogel is improved with the assistance of CNT-rGO network. In addition, with CNT-rGO, the charge transfer resistance is reduced from 997.3 Ω for commercial WS_2 powder to 620.5 Ω for WS_2/CNT-rGO-200 aerogel electrode as evaluated by EIS measurement (Figure S12, Supporting Information) and the fitted values shown in Table S3 (Supporting Information).

The cycle stability and rate capability of WS_2/CNT-rGO-200 aerogel is comparable or better than the state-of-art values reported recently for many WS_2 based hybrid anodes of LIBs, and even for TMDs anodes (i.e., MoS_2) of SIBs, especially at high current densities of 2000, 5000, and 10 000 mA g^{-1} as summarized in Table S4a,b (Supporting Information), respectively. Such a superior performance of WS_2/CNT-rGO aerogel can be attributed to synergistic effect between the WS_2 nanosheets and CNT-rGO network, and the special designed 3D ordered microchannel structures which offers several advantages compared to the bulk structure. First, WS_2 nanosheets/nanoflowers firmly waved by CNT network based on rGO aerogel structure, which not only provides the carbon matrix to support the growth backbone for WS_2 nanostructure, but also provides excellent conductivity to improve the electron transfer rate. Second, the rigid CNT network prevents the aggregation of rGO leading to a rigid nanoarchitecture to inhibit the WS_2 restacking issue and mechanical failure during the lithaition/delithiation and sodiation/desodiation cycles, leading to stable cycling performance. Third, thin layered structure of WS_2 nanosheets can provide a large surface area and defect sites, leading to an enhanced lithium/sodium ion accessibility and reduce the lithium/sodium ion diffusion length. Fourth, free-standing 3D ordered microchannel structure design may further affect the lithium/sodium kinetic behavior. Owing to these advantages, the binder free WS_2/CNT-rGO aerogel nanostructure exhibit high capacity, excellent rate capability and cycling stability both for LIBs and SIBs. Moreover, we also note that the performance and cost, including materials and battery production and recycling, should be further optimized and considered when scaled up used in grid level energy storage applications.[68]

3. Conclusions

Hybrid WS_2/CNT-rGO aerogels with 3D ordered microchannel structures were synthesized by a simple solvothermal method followed by freeze-drying and post annealing process. The ordered 3D structures were formed by ice template during the freeze-drying process. Such a 3D structure network with ordered microchannels not only can provide ionic conductive channels for the electrolyte to penetrate into the active electrode, the conductive CNT-rGO wall also can provide effective electronic transportation routes, leading to an enhanced electrochemical performance as the anode electrodes both for LIBs and SIBs. WS_2/CNT-rGO aerogel nanocomposites can deliver specific capacities of 749 and 311.4 mA h g^{-1} at a current density of 100 mA g^{-1} as the anode materials of LIBs and SIBs, respectively. The excellent electrochemical performance has been attributed to the synergistic effect between the WS_2 nanosheets and CNT-rGO network, and the special designed unique 3D ordered microchannel nanoarchictures.

4. Experimental Section

Synthesis of WS_2/CNT-rGO Aerogel Nanostructure: WS_2/CNT-rGO aerogel nanostructures were synthesized via a simple solvothermal method followed by the freeze drying and post annealing process. GO was synthesized by a modified Hummer's method.[56,69] CNTs dissolved in N-methyl pyrrolidone (NMP) solution were purchased from Timesnano Company directly. In a typical process, GO (40 mg) and thoroughly dispersed into DMF (20 mL) with probe sonication for 40 min followed by adding CNT (8 mg) and sonicated for 20 min to fully disperse CNT into GO solution. Then, various masses of $(NH_4)_2WS_4$ powders (100, 200, and 300 mg) were added into the mixed solution and continuously stirred for about 30 min at room temperature. The prepared solution was then transferred to a Teflon-lined stainless steel autoclave (50 mL), sealed and kept in a normal lab oven at 200 °C for 10 h. After solvothermal growth, cylindrical shape of hydrogel was collected and rinsed with DMF and DI water for several times to remove unreacted chemicals and DMF residue. The second step is the structure formation process. In brief, the collected hydrogel was fast froze in liquid nitrogen and then freeze dried in a freeze dryer with vacuum at −70 °C for 48 h. The final product was annealed at 500 °C for 2 h in H_2/N_2 (5%/95%) gas flow to remove the sulfur residue and increase the crystallinity of the sample. The control sample of pure CNT-rGO aerogel was synthesized without adding $(NH_4)_2WS_4$ powder.

Material Characterization: The morphologies study of the WS_2/CNT-rGO aerogel nanostructures was performed by field-emission scanning electron microscopy (FESEM, JSM-7600F, JEOL, Tokyo, Japan) and transmission electron microscopy (TEM, JEM-2100F, JEOL, Tokyo, Japan). Crystal structure of the synthesized nanocomposites was examined by XRD (Bruker D8 advance, Karlsruhe, Germany) with Cu Ka ($\lambda = 0.154$ nm) radiation under the accelerating voltage of 40 kV. Raman spectra were measured by a confocal Raman system with the 532 nm laser excitation (WITec Instruments Corp., Ulm, Germany). The content of WS_2 in aerogels was carried out by TGA (DTG-60, Shimadzu, Kyoto, Japan).

Battery Assembly and Electrochemical Measurements: The electrochemical performance of WS_2/CNT-rGO nanocomposites was evaluated by a half-cell testing configuration based on the CR2032 coin cell. WS_2/CNT-rGO aerogel was cut into round shape and used as the working electrode without any additives or binders. A lithium/sodium foil was employed as the counter electrode. For LIBs, 1 M $LiPF_6$ dissolved into ethylene-carbonate/diethyl-carbonate (EC/DEC) solution (1:1, v:v) was used as the electrolyte. For SIBs, 1 M $NaPF_6$ dissolved into EC/DEC solution (1:1, v:v) with 2% fluoroethylene-carbonate (FEC, stabilizer)

was used as the electrolyte. A Celgard 2400 membrane and a glass Fiber Filter (GB-100R, Advantec, Japan) were used as the membranes of LIBs and SIBs, respectively. The commercial WS_2 powder was mixed with conductive carbon black and polyvinylidene fluoride (PVDF) binder in a weight ratio of 80:10:10 and added with several drops of NMP solution to form a slurry. The slurry was then coated onto Ni foam and dried in a vacuum oven at 120 °C overnight. All components listed above were assembled into a standard CR2032 coin cell in a glove box filled with argon gas with the oxygen and moisture level lower than 1 ppm. Electrochemical measurements were carried out after 24 h of battery assembly. CV and EIS measurements were performed by an electrochemical workstation (VMP3, Bio-Logic, Claix, France). The galvanostatic charge/discharge test was measured in the voltage range of 0.01–3 V at various current densities ranging from 100 to 10 000 mA g^{-1} using a battery analyzer (Neware, Shenzhen, China).

Supporting Information

Supporting Information is available from the Wiley Online Library or from the author.

Acknowledgements

This work was financially supported by SUTD Digital Manufacturing and Design [DManD] Centre.

Received: May 20, 2016
Revised: July 4, 2016
Published online: August 5, 2016

[1] J. M. Tarascon, M. Armand, *Nature* **2001**, *414*, 359.
[2] A. S. Aricò, P. Bruce, B. Scrosati, J.-M. Tarascon, W. Van Schalkwijk, *Nat. Mater.* **2005**, *4*, 366.
[3] P. G. Bruce, S. A. Freunberger, L. J. Hardwick, J. M. Tarascon, *Nat. Mater.* **2012**, *11*, 19.
[4] B. Dunn, H. Kamath, J. M. Tarascon, *Science* **2011**, *334*, 928.
[5] S. W. Kim, D. H. Seo, X. Ma, G. Ceder, K. Kang, *Adv. Energy Mater.* **2012**, *2*, 710.
[6] N. Yabuuchi, K. Kubota, M. Dahbi, S. Komaba, *Chem. Rev.* **2014**, *114*, 11636.
[7] L. David, R. Bhandavat, U. Barrera, G. Singh, *Nat. Commun.* **2016**, *7*, 10998.
[8] H. Pan, Y.-S. Hu, L. Chen, *Eng. Environ. Sci.* **2013**, *6*, 2338.
[9] Y. Dong, S. Li, K. Zhao, C. Han, W. Chen, B. Wang, L. Wang, B. Xu, Q. Wei, L. Zhang, *Eng. Environ. Sci.* **2015**, *8*, 1267.
[10] M. D. Slater, D. Kim, E. Lee, C. S. Johnson, *Adv. Funct. Mater.* **2013**, *23*, 947.
[11] M. Reddy, G. Subba Rao, B. Chowdari, *Chem. Rev.* **2013**, *113*, 5364.
[12] D. Chao, C. Zhu, X. Xia, J. Liu, X. Zhang, J. Wang, P. Liang, J. Lin, H. Zhang, Z. X. Shen, *Nano Lett.* **2014**, *15*, 565.
[13] L. Peng, Y. Zhu, D. Chen, R. S. Ruoff, G. Yu, *Adv. Energy Mater.* **2016**, *6*, 1600025.
[14] D. Kundu, E. Talaie, V. Duffort, L. F. Nazar, *Angew. Chem. Int. Ed.* **2015**, *54*, 3431.
[15] Z.-S. Wu, G. Zhou, L.-C. Yin, W. Ren, F. Li, H.-M. Cheng, *Nano Energy* **2012**, *1*, 107.
[16] V. Etacheri, R. Marom, R. Elazari, G. Salitra, D. Aurbach, *Eng. Environ. Sci.* **2011**, *4*, 3243.
[17] L. W. Ji, Z. Lin, M. Alcoutlabi, X. W. Zhang, *Eng. Environ. Sci.* **2011**, *4*, 2682.
[18] S. Hy, H. Liu, M. Zhang, D. Qian, B.-J. Hwang, Y. S. Meng, *Eng. Environ. Sci.* **2016**, *9*, 1931.
[19] C. Zhu, P. Kopold, W. Li, P. A. van Aken, J. Maier, Y. Yu, *Adv. Sci* **2015**, *2*, 1500200.
[20] C. Tan, H. Zhang, *Chem. Soc. Rev.* **2015**, *44*, 2713.
[21] C. Zhu, X. Mu, P. A. van Aken, Y. Yu, J. Maier, *Angew. Chem. Int. Ed.* **2014**, *53*, 2152.
[22] C. Zhu, X. Mu, P. A. van Aken, J. Maier, Y. Yu, *Adv. Energy Mater.* **2015**, *5*, 1401170.
[23] X. Xu, W. Liu, Y. Kim, J. Cho, *Nano Today* **2014**, *9*, 604.
[24] X. Rui, H. Tan, Q. Yan, *Nanoscale* **2014**, *6*, 9889.
[25] C. Zhang, Z. Ning, Y. Liu, T. Xu, Y. Guo, A. Zak, Z. Zhang, S. Wang, R. Tenne, Q. Chen, *Appl. Phys. Lett.* **2012**, *101*, 113112.
[26] R. Chen, T. Zhao, W. Wu, F. Wu, L. Li, J. Qian, R. Xu, H. Wu, H. M. Albishri, A. S. Al-Bogami, *Nano Lett.* **2014**, *14*, 5899.
[27] C. Liu, F. Li, L. P. Ma, H. M. Cheng, *Adv. Mater.* **2010**, *22*, E28.
[28] Y. G. Guo, J. S. Hu, L. J. Wan, *Adv. Mater.* **2008**, *20*, 2878.
[29] C. Zhu, P. Kopold, P. A. van Aken, J. Maier, Y. Yu, *Adv. Mater.* **2016**, *28*, 2409.
[30] H. Zhang, X. Yu, P. V. Braun, *Nat. Nanotechnol.* **2011**, *6*, 277.
[31] S. Chabi, C. Peng, D. Hu, Y. Zhu, *Adv. Mater.* **2014**, *26*, 2440.
[32] S. Nardecchia, M. C. Serrano, M. C. Gutiérrez, M. T. Portolés, M. L. Ferrer, F. del Monte, *Adv. Funct. Mater.* **2012**, *22*, 4411.
[33] M. C. Gutiérrez, M. L. Ferrer, F. del Monte, *Chem. Mater.* **2008**, *20*, 634.
[34] D. Chen, G. Ji, B. Ding, Y. Ma, B. Qu, W. Chen, J. Y. Lee, *Nanoscale* **2013**, *5*, 7890.
[35] H. Hu, Z. Zhao, W. Wan, Y. Gogotsi, J. Qiu, *Adv. Mater.* **2013**, *25*, 2219.
[36] A. Cao, Z. Liu, S. Chu, M. Wu, Z. Ye, Z. Cai, Y. Chang, S. Wang, Q. Gong, Y. Liu, *Adv. Mater.* **2010**, *22*, 103.
[37] Z. Lin, Z. Zeng, X. Gui, Z. Tang, M. Zou, A. Cao, *Adv. Energy Mater.* **2016**, *6*, 16000554.
[38] S. Nardecchia, D. Carriazo, M. L. Ferrer, M. C. Gutiérrez, F. del Monte, *Chem. Soc. Rev.* **2013**, *42*, 794.
[39] H. Liu, D. Su, G. Wang, S. Z. Qiao, *J. Mater. Chem.* **2012**, *22*, 17437.
[40] Y. G. Zhu, Y. Wang, Y. Shi, J. I. Wong, H. Y. Yang, *Nano Energy* **2014**, *3*, 46.
[41] Z. Y. Zeng, Z. Y. Yin, X. Huang, H. Li, Q. Y. He, G. Lu, F. Boey, H. Zhang, *Angew. Chem. Int. Ed.* **2011**, *50*, 11093.
[42] M. A. Worsley, S. J. Shin, M. D. Merrill, J. Lenhardt, A. J. Nelson, L. Y. Woo, A. E. Gash, T. F. Baumann, C. A. Orme, *ACS Nano* **2015**, *9*, 4698.
[43] A. Ferrari, J. Meyer, V. Scardaci, C. Casiraghi, M. Lazzeri, F. Mauri, S. Piscanec, D. Jiang, K. Novoselov, S. Roth, *Phys. Rev. Lett.* **2006**, *97*, 187401.
[44] S. Eigler, A. Hirsch, *Angew. Chem. Int. Ed.* **2014**, *53*, 7720.
[45] D. R. Dreyer, S. Park, C. W. Bielawski, R. S. Ruoff, *Chem. Soc. Rev.* **2010**, *39*, 228.
[46] A. C. Ferrari, *Solid State Commun.* **2007**, *143*, 47.
[47] Y. Wang, Z. J. Han, S. F. Yu, R. R. Song, H. H. Song, K. K. Ostrikov, H. Y. Yang, *Carbon* **2013**, *64*, 230.
[48] Y. Wang, S. F. Yu, C. Y. Sun, T. J. Zhu, H. Y. Yang, *J. Mater. Chem.* **2012**, *22*, 17584.
[49] S. H. Choi, Y. C. Kang, *Nanoscale* **2015**, *7*, 3965.
[50] Y. Liu, W. Wang, H. Huang, L. Gu, Y. Wang, X. Peng, *Chem. Commun.* **2014**, *50*, 4485.
[51] W. Yang, J. Wang, C. Si, Z. Peng, J. Frenzel, G. Eggeler, Z. Zhang, *J. Mater. Chem. A* **2015**, *3*, 17811.
[52] Y. Liu, W. Wang, Y. Wang, X. Peng, *Nano Energy* **2014**, *7*, 25.
[53] K. Shiva, H. S. S. R. Matte, H. B. Rajendra, A. J. Bhattacharyya, C. N. R. Rao, *Nano Energy* **2013**, *2*, 787.
[54] Y. Wang, F. Yan, S. W. Liu, A. Y. S. Tan, H. Song, X. W. Sun, H. Y. Yang, *J. Mater. Chem. A* **2013**, *1*, 5212.

[55] Y. Wang, G. Xing, Z. Han, Y. Shi, J. I. Wong, Z. X. Huang, K. Ostrikov, H. Yang, *Nanoscale* **2014**, *6*, 8884.
[56] Y. Wang, Z. X. Huang, Y. Shi, J. I. Wong, M. Ding, H. Y. Yang, *Sci. Rep.* **2015**, *5*, 9164.
[57] L. David, R. Bhandavat, U. Barrera, G. Singh, *Sci. Rep.* **2015**, *5*, 9792.
[58] R. Bhandavat, L. David, G. Singh, *J. Phys. Chem. Lett.* **2012**, *3*, 1523.
[59] J. Cabana, L. Monconduit, D. Larcher, M. R. Palacin, *Adv. Mater.* **2010**, *22*, E170.
[60] W. Dreyer, J. Jamnik, C. Guhlke, R. Huth, J. Moškon, M. Gaberšček, *Nat. Mater.* **2010**, *9*, 448.
[61] D. Xiong, X. Li, H. Shan, B. Yan, L. Dong, Y. Cao, D. Li, *J. Mater. Chem. A* **2015**, *3*, 11376.
[62] Y. Liu, A. Palmieri, J. He, Y. Meng, N. Beauregard, S. L. Suib, W. E. Mustain, *Sci. Rep.* **2016**, *6*, 25860.
[63] S.-Y. Liu, J. Xie, Y.-X. Zheng, G.-S. Cao, T.-J. Zhu, X.-B. Zhao, *Electrochim. Acta* **2012**, *66*, 271.
[64] Y. Wang, B. Chen, D. H. Seo, Z. J. Han, J. I. Wong, K. K. Ostrikov, H. Zhang, H. Y. Yang, *NPG Asia Mater.* **2016**, *8*, e268.
[65] C. Zhu, P. Kopold, W. Li, P. A. van Aken, J. Maier, Y. Yu, *J. Mater. Chem. A* **2015**, *3*, 20487.
[66] Y. Liu, N. Zhang, H. Kang, M. Shang, L. Jiao, J. Chen, *Chem. - Eur. J.* **2015**, *21*, 11878.
[67] D. Su, S. Dou, G. Wang, *Chem. Commun.* **2014**, *50*, 4192.
[68] D. Larcher, J. Tarascon, *Nat. Chem.* **2015**, *7*, 19.
[69] W. S. Hummers, R. E. Offeman, *J. Am. Chem. Soc.* **1958**, *80*, 1339.

